



# Spherical nickel doped cobalt phosphide as an anode catalyst for oxygen evolution reaction in alkaline media: From catalysis to system

Deok-Hye Park<sup>a</sup>, Min-Ha Kim<sup>a</sup>, Myungjae Kim<sup>b</sup>, Jeong-Hyeon Byeon<sup>a</sup>, Jae-Sung Jang<sup>a</sup>,  
Ji-Hwan Kim<sup>a</sup>, Da-Mi Lim<sup>a</sup>, Seon-Ha Park<sup>a</sup>, Yun-Hui Gu<sup>a</sup>, Jiwoong Kim<sup>b,\*</sup>, Kyung-Won Park<sup>a,\*</sup>

<sup>a</sup> Department of Chemical Engineering, Soongsil University, Seoul 06978, Republic of Korea

<sup>b</sup> Department of Organic Materials and Fiber Engineering, Soongsil University, Seoul 06978, Republic of Korea

## ARTICLE INFO

### Keywords:

Anion exchange membrane water electrolysis  
Oxygen evolution reaction  
Anode catalyst  
Nickel doped cobalt phosphide

## ABSTRACT

Anion exchange membrane water electrolysis (AEMWE) uses a zero-gap membrane-electrode-assembly (MEA) consisting of a polymer electrolyte membrane and non-precious metal-based catalysts. However, anode catalysts for the oxygen evolution reaction (OER), which is the rate-determining-step in WE, need to be intensively developed to achieve superior electrocatalytic activity and stability. Herein, we report the synthesis and characterization (experimental and simulation) of spherical Ni-doped (5–15 at%) cobalt phosphide (Ni-CoP) as the anode catalyst for the OER. Specifically, the DFT calculation exhibited that the addition of Ni in CoP might increase the energy density in the Fermi level of pristine CoP, enhance the charge transfer rate during the OER, and reduce the energy barrier for the formation of OOH\*, thereby boosting the OER activity. The prepared Ni-doped CoP catalyst was directly loaded onto a foam-type Ni-based gas diffusion layer for effective application in AEMWE. It was found that the electrocatalytic activity of the AEMWE depends on the porosity of the NFs as catalyst substrates. The unit cell containing the membrane-electrode-assembly fabricated with NCP-10 delivered a high current density of 1.12 A cm<sup>-2</sup> at 1.8 V and a low reduction rate of 0.64 mA cm<sup>-2</sup> h<sup>-1</sup> for 250 h.

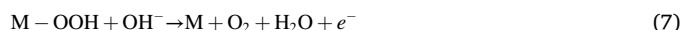
## 1. Introduction

Water electrolysis (WE) is an ecofriendly electrochemical process for efficiently converting water into hydrogen gas, as a clean fuel [1,2]. In WE, representative types of electrolytes are -acidic and alkaline media [3,4]. In particular, for alkaline water electrolysis (AWE), in which an alkaline medium is used as an electrolyte, the oxygen evolution reaction (OER; Eq. (1)) and hydrogen evolution reaction (HER; Eq. (2)) occur at the anode and cathode, respectively, as follows [4]:



Generally, the thermodynamic standard potential ( $E^\circ$ ) required for the overall reaction (Eq.(3)) in AWE is 1.23 V [3]. However, in practice, hydrogen production commences at an overpotential of more than 1.23 V because of the slow electrochemical reactions [4]. The OER is

slower than the HER because of its sluggish kinetics and complex reaction steps (Eqs. (4)–(7)) and is expected to be the main cause of the high overpotential required for AWE [5].



To effectively reduce the overpotential in AWE, highly efficient anode catalysts for OER need to be developed. To date, precious metal oxides, such as IrO<sub>2</sub> and RuO<sub>2</sub>, have been used as anode catalysts, exhibiting superior electrocatalytic activity for the OER [6]. However, their high cost, scarcity, and low stability are the main obstacles in the commercialization of WE [6]. Thus, various transition metal-based structures such as oxides, carbides, nitrides, phosphides, phosphates, sulfides, chalcogenides, and perovskites, have been studied to replace precious metal-based catalysts [3,5,7–12]. Among these non-precious

\* Corresponding authors.

E-mail addresses: [jwk@ssu.ac.kr](mailto:jwk@ssu.ac.kr) (J. Kim), [kwpark@ssu.ac.kr](mailto:kwpark@ssu.ac.kr) (K.-W. Park).

<https://doi.org/10.1016/j.apcatb.2023.122444>

Received 15 November 2022; Received in revised form 17 January 2023; Accepted 8 February 2023

Available online 10 February 2023

0926-3373/© 2023 Elsevier B.V. All rights reserved.

metal anode catalysts, transition metal phosphides (TMPs) have recently received considerable attention owing to their non-toxicity, low cost, high electrical conductivity, excellent chemical and thermal stability, high mechanical strength, and stability in alkaline media [8,10,13–16]. Recently, heteroatom-doped metal phosphides, rather than mono-metal phosphides, have been extensively studied as OER catalysts, and improved catalytic activities due to modified electronic structures have been observed. Han et al. reported that a bimetallic phosphide embedded in N and P co-doped porous carbon has a low overpotential of 236 mV at 10 mA cm<sup>-2</sup> in 1 M KOH because of the synergistic effect of the bimetallic phosphide structure and co-doping of N and P [17]. Mu et al. synthesized flower like Ru-doped NiCoP on NF with improved water-splitting performance (10 mA cm<sup>-2</sup> at 1.515 V), which was attributed to the accelerated electron transport caused by Ru doping and a high number of active sites resulting from the specific electrode morphology [18]. Furthermore, shape-controlled catalysts and electrodes for high-performance electrochemical applications including WE have been studied using metal-organic frameworks [19–22].

Recently, in addition to the formation of TMPs via homogenous nucleation, TMPs directly grown on electrically conductive substrates, such as nickel and stainless steel foams, have been studied [23]. These particular electrode structures could significantly increase the utilization of electrocatalytically active sites and enhance the emission of gas products generated during the electrochemical reactions in WE systems [24]. Yi et al. reported that CoFeP nanotube-arrays formed on nickel foam (NF) via phosphidation using a metal organic framework have excellent OER performance (an overpotential of 253 mV for 10 mA cm<sup>-2</sup>) [25]. However, it is difficult to measure their intrinsic electrocatalytic properties of catalysts directly formed on porous substrates because of the various parameters related to the specific electrode structures [23]. In practice, the electrochemical performance of catalysts on foam-type substrates may depend on the fabrication method. Furthermore, the electrochemical performance of catalysts on porous substrates based on apparent areas could be overestimated owing to the uncertainties in measuring the specific surface areas of the substrates [26].

In this study, powder-type CoP catalysts doped with 0–15 at% Ni (NCP-0, 5, 10, and 15) were prepared to accurately investigate the influence of Ni doping on the electrocatalytic activity of CoP. First, spherical Ni-containing cobalt glycerate (NCG) was prepared as a precursor using hydrothermal synthesis. The NCP catalyst was obtained via phosphidation using the NCG precursor and NaH<sub>2</sub>PO<sub>2</sub> (400 °C under a N<sub>2</sub> atmosphere for 3 h). Among these catalysts, NCP-10 exhibited the best electrocatalytic activity for the OER, owing to its enhanced electron transport and higher electrochemically active area. Furthermore, NCP catalysts were directly formed on NF substrates using the same phosphidation process as that used for NCP-X (NCP-X/NF) for long-term stability and single cell tests. A membrane electrode assembly (MEA) for anion exchange membrane water electrolysis (AEMWE) was fabricated using NCP-X/NF. Compared with IrO<sub>2</sub> formed on NF via dip-coating, NCP-10/NF exhibited improved OER performance with an overpotential of 316 mV at 10 mA cm<sup>-2</sup> and stability for 220 h. NCP-10 anode catalysts formed on three-types of NFs with different porosities (high-porosity NF (HPNF), medium-porosity NF (MPNF), and low-porosity NF (LPNF)) were prepared to investigate the effect of the substrate porosity on the performance of the AEMWE system. NCP-10/MPNF delivered the highest OER activity (1.12 A cm<sup>-2</sup> at 1.8 V). By contrast, NCP-10/LPNF showed an initial drastic reduction in performance and high retention (0.64 mA cm<sup>-2</sup> h<sup>-1</sup> for 250 h).

## 2. Experimental section

### 2.1. Reagents

Nickel nitrate hexahydrate (Ni(NO<sub>3</sub>)<sub>2</sub>·6 H<sub>2</sub>O, 99%), cobalt nitrate hexahydrate (Co(NO<sub>3</sub>)<sub>2</sub>·6H<sub>2</sub>O, 99%), Isopropyl alcohol (IPA, >99%),

sodium hypophosphite monohydrate (NaH<sub>2</sub>PO<sub>2</sub>·H<sub>2</sub>O, >99%), absolute ethanol (CH<sub>3</sub>CH<sub>2</sub>OH, >99.5%), and glycerol solution (99%) were purchased from Sigma-Aldrich Co. (USA). Hydrochloric acid (HCl, 36%, grade T) was purchased from SAMCHUN Chemical Co. (Korea). NF-type materials with porosities of ≥ 95% and < 20% were purchased from MTI corporation (Seoul, Korea).

### 2.2. Synthesis of spherical NCG precursors

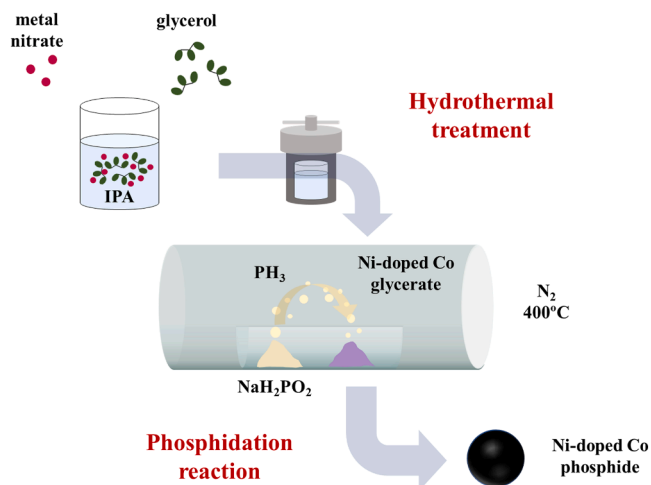
To prepare spherical Ni-doped Co<sub>3</sub>O<sub>4</sub> powders, Ni(NO<sub>3</sub>)<sub>2</sub>·6 H<sub>2</sub>O and Co(NO<sub>3</sub>)<sub>2</sub>·6 H<sub>2</sub>O with Ni ratios of 0, 5, 10, and 15 at% were dissolved in a mixture of isopropyl alcohol and glycerol with continuous stirring for 1 h (Scheme 1) [27]. The completely dissolved metal salt solutions were transferred to a Teflon-lined stainless-steel autoclave and heated at 180 °C for 8 h. The resulting precipitates were washed several times using a centrifuge with ethanol to obtain NCG-X samples (X = 0, 5, 10, and 15).

### 2.3. Synthesis of NCP catalysts

The precursors were placed into a tube furnace with NaH<sub>2</sub>PO<sub>2</sub> (as the source of phosphide) and heated at 400 °C under N<sub>2</sub> atmosphere for 3 h. During heating, the NCG precursors were phosphidized by PH<sub>3</sub> produced with an upstream of NaH<sub>2</sub>PO<sub>2</sub> to yield NCP-X samples (X = 0, 5, 10, and 15).

### 2.4. Synthesis of NCP/NF catalysts

NCP-X deposited on NF was prepared to evaluate the OER performance of NCP-X as an anode catalyst in a single cell test. NF materials with porosities of 80.0%, 48.5%, and 33.1% were used as catalyst layers. First, the NF was sonicated in 1.0 M HCl for 10 min to remove impurities and nickel oxide phases, and then dried overnight in a vacuum oven. The pretreated NF was placed into a metal precursor solution containing Ni (NO<sub>3</sub>)<sub>2</sub>·6 H<sub>2</sub>O and Co(NO<sub>3</sub>)<sub>2</sub>·6 H<sub>2</sub>O dissolved in a mixture of isopropyl alcohol and glycerol, and then stirred for 1 h. The metal precursor solution with NF was transferred into an autoclave and heated at 180 °C for 8 h. NF was reacted with the metal precursor solution and dried in an oven at 50 °C for 24 h. The dried NF was placed with NaH<sub>2</sub>PO<sub>2</sub> as the phosphide source in a tube furnace and heated at 400 °C under N<sub>2</sub> atmosphere for 3 h. The resulting sample was NCP-10/NF, with NCP-10 directly formed and deposited on NF (Fig. 5(a)).



**Scheme 1.** Schematic illustration of the synthesis method for NCP-X catalysts.

## 2.5. Structural analysis of anode catalysts

X-ray diffraction (XRD) measurements were performed using a D2 Phaser (Bruker AXS, USA, 30 kV) with a Cu K $\alpha$  radiation source ( $\lambda = 1.5418 \text{ \AA}$ ). The morphology and size of the samples were confirmed using field-emission scanning electron microscopy (FE-SEM, Gemini 300, ZEISS). Elemental mapping was performed using energy dispersive X-ray spectroscopy (EDS, Bruker). The chemical states of the samples were observed using X-ray photoelectron spectroscopy (XPS, K-alpha, Thermo Scientific Inc.) with an Al K $\alpha$  X-ray source (1486.6 eV). The metal compositions of the samples were measured using inductively coupled plasma-optical emission spectroscopy (ICP-OES, PerkinElmer Optima 8300). Porosity analysis was conducted using a mercury porosimeter (PM33GT; Quantachrome, USA).

## 2.6. Electrochemical analysis of anode catalysts

The electrochemical properties of the catalysts were evaluated using a potentiostat (VSP; BioLogic Science Instruments, France) in a three-electrode electrochemical cell. Glassy carbon (GC, a diameter of 5 mm) and single junction mercury oxide (Hg/HgO) were used as the working and reference electrodes, respectively. Pt wire and graphitic rod were used as counter electrodes for powder-type catalysts and catalysts loaded on NF, respectively. All measured potentials were converted into a reversible hydrogen electrode (RHE) as follows:  $E_{\text{RHE}} = E_{\text{Hg/HgO}} + 0.0591 \times \text{pH} + 0.098$ . The catalyst inks for electrochemical analysis were prepared with 30 mg of the catalyst, 30  $\mu\text{L}$  of Fumion FAA-3-Br (10 wt% in N-Methyl-2-pyrrolidone, FuMA-Tech, Germany) as a binder, and 150  $\mu\text{L}$  of absolute ethanol as a solvent. The total catalyst loading on the GC electrode was  $\sim 400 \mu\text{g cm}^{-2}$ . Prior to the OER measurements, cyclic voltammetry (CV) was performed in Ar-saturated 1 M KOH in the potential range of 0.1–1.3 V at a scan rate of  $50 \text{ mV s}^{-1}$  for 50 cycles to sufficiently activate the catalyst. After the stabilization of the catalyst, linear sweep voltammetry (LSV) for OER was conducted three times to get rid of oxygen species; rotation speed of 1600 rpm; potential range of 1.0–1.7 V; and scan rate of  $5 \text{ mV s}^{-1}$ . The electrochemically active surface area (ECSA) values of the catalysts were determined from the double layer capacitance ( $C_{\text{dl}}$ ) measured at various scan rates of 5–80  $\text{mV s}^{-1}$  in the potential range of 0.8–1.0 V vs RHE as follows:  $\text{ECSA} = C_{\text{dl}}/C_s$  ( $C_s$  is  $\sim 0.04 \text{ mF cm}^{-2}$  in 1 M KOH) [28]. Electrochemical impedance spectroscopy (EIS) measurements were performed in a frequency range of 100 kHz to 0.1 Hz at 1.6 V vs. RHE with an amplitude of 10 mV. Stability tests with 4  $\text{mg cm}^{-2}$  of a catalyst dip-coated onto a NF substrate were conducted using chronoamperometry at a constant current density of  $20 \text{ mA cm}^{-2}$  for 220 h.

## 2.7. MEA fabrication and single-cell measurements

The MEA was fabricated using a commercial gas diffusion electrode (20% Pt/C on carbon paper, Fuel Cell Earth) as the cathode, a pretreated AEM (FAA-3-50, FuMA-Tech, Germany), and catalyst-loaded Pt-coated NF as the anode. The Pt coating on the acid-treated NF was applied using a radio frequency magnetron sputtering system operated at a sputtering power of 50 W under an Ar flow of  $30 \text{ cm}^3 \text{ min}^{-1}$ . The MEAs were prepared by directly coating the catalyst onto a membrane or by hot-pressing with a catalyst-loaded NF substrate and membrane. To prevent pinholes from being generated on the membrane using the NF substrate, 10 wt% anion exchange ionomers (FAA-3-Br-10 wt% in NMP, FuMA-Tech, Germany) with respect to an amount of catalyst was coated on NCP-10/NF by ultrasonic spraying (BE-CT-1901–400, Boyaz Energy Co., Korea) and then dried at  $50^\circ\text{C}$  for 24 h. Hot-pressing was conducted at  $50^\circ\text{C}$  under a pressure of 50 bar for 2 min. The thickness of the gaskets was  $\sim 90\%$  of that of the MEA before pressing. After hot-pressing, a single cell was assembled with separators and end plates at a torque of 7.91 N·m. Then, 1 M KOH solution was supplied to the assembled single cell at a flow rate of  $5 \text{ mL min}^{-1}$ . The WE performance

of the single cell was recorded at various cell temperatures using a potentiostat (HCP-803, Bio-Logic Science Instruments, France). The WE activity test was conducted using LSV in the potential range of 1.2–2.0 V at a scan rate of  $5 \text{ mV s}^{-1}$ . Prior to the WE test, CV was performed in the potential range of 0.1–1.3 V at a scan rate of  $50 \text{ mV s}^{-1}$ . The stability test was performed using chronoamperometry at a constant potential of 1.8 V at  $50^\circ\text{C}$  for 250 h. EIS was performed over the frequency range of 10 kHz–100 mHz at 1.6 V with an amplitude of 10 mV. For lithium-ion exchange membrane water electrolysis (LEMWE), NCP-10/NF was used as an anode catalyst and a lithium-ion conducting membrane (Boyaz Energy Co., Korea) was used. 4 M LiOH solution was supplied to the anode and cathode of the LEMWE [29].

## 2.8. Calculation methods and details

Density functional theory (DFT) simulations were performed using the Vienna ab initio simulation package [30]. The exchange–correlation energy was represented by the generalized gradient approximation with the Perdew–Burke–Ernzerhof functional [31,32]. The ion–electron interaction was described using the projector-augmented wave method [33]. A cutoff energy of 500 eV was used to optimize the structure of the bulk and surface models. All calculations were performed using spin–polarization. Based on the current experimental results, (211) surface models were constructed to describe the OER reactions. A vacuum slab of  $15 \text{ \AA}$  was used to prevent vertical interactions with the reaction surface. Brillouin zone integration was performed using  $13 \times 13 \times 13$  and  $3 \times 3 \times 1$  Monkhorst–Pack grids for the CoP bulk and (211) surface models, respectively. The following equations were used to calculate the surface energy convergence with a slab thickness of 3–10 layers:

$$E_s = (E_{\text{Slab}} - N \cdot E_{\text{Bulk}}) / 2A \quad (8)$$

Here,  $E_{\text{Slab}}$  and  $E_{\text{Bulk}}$  are the optimized slab and bulk total energies, respectively;  $N$  is the number of bulk units contained in the slab; and  $A$  is the surface area of the slab. In addition, the most suitable adsorption sites, such as the hollow, top, and bridge, for the  $^*\text{OH}$ ,  $^*\text{O}$ , and  $^*\text{OOH}$  species in the (211) surface model were investigated. Then, optimal OER pathway, depending on the Ni content of the surface model, was examined. For the OER process, based on the standard hydrogen electrode, the change in the reaction free energy ( $\Delta G$ ) was estimated for each elementary step using the following equation:

$$\Delta G = \Delta E + \Delta \text{ZPE} - T\Delta S - eU - kT \ln 10 \times \text{pH} \quad (9)$$

Here,  $\Delta$  indicates the difference in the parameter between the previous and current reaction steps in the electronic energy  $E$ , zero–point energy (ZPE), and entropy  $S$ , where  $U$  is the applied potential. The reaction temperature was fixed at  $300 \text{ K}$ . The  $\Delta \text{ZPE}$  and  $\Delta S$  values were referred to previously reported data [34].

## 3. Results and discussion

### 3.1. Synthesis procedure of and structural analysis of NCP-X catalysts

XRD patterns and FTIR spectra of the spherical precursors (NCG-X) prepared using a hydrothermal process were obtained to confirm the crystallinity and surface organic compounds (Fig. S1). The NCG-X precursors exhibit the broad XRD patterns with the characteristic peaks at  $10.8^\circ$ ,  $19.2^\circ$ ,  $35.3^\circ$ , and  $60^\circ$ , which represent that the as-prepared precursors are metal glycerates (Fig. S1(a)) [35–37]. The IR bands at 3420, 2861, 1661, and  $1593 \text{ cm}^{-1}$  correspond to O–H, C–H, C=O, and C=C stretching vibrations, respectively [35–38]. Furthermore, C–H bending ( $1415 \text{ cm}^{-1}$ ), C–O stretching ( $1115 \text{ cm}^{-1}$ ), C–C stretching ( $1055 \text{ cm}^{-1}$ ), and plane C–H bending vibration ( $807 \text{ cm}^{-1}$ ) modes are observed [35–38]. The peaks at  $\sim 600 \text{ cm}^{-1}$  indicate M–O (M = cobalt or nickel) [35–38]. Hence, the XRD and FTIR results represent that all the as-prepared precursors are metal glycerate structures. The NCG-10

precursor prepared for the NCP-10 was quite spherical, with an average diameter of  $\sim 650$  nm and homogeneous distribution of Ni, Co, C, and O without any agglomeration, indicating a well-mixed solid solution (Fig. S2). The Ni-Co glycerate nanospheres were previously shown to form during a hydrothermal process with glycerol-decomposed glycerate ( $\text{C}_3\text{H}_5\text{O}_4^-$ ) and  $\text{Ni}^{2+}/\text{Co}^{2+}$  dissolved in isopropyl alcohol [39]. The precursor was placed with  $\text{NaH}_2\text{PO}_2$  as the phosphide source into a tube furnace and heated at  $400^\circ\text{C}$  under an  $\text{N}_2$  atmosphere. During the heating, NCG-10 was easily phosphidized by the  $\text{PH}_3$  produced with an upstream of  $\text{NaH}_2\text{PO}_2$ , forming NCP-10 as the OER anode catalyst (Scheme 1).

Fig. 1(a) shows SEM and EDS images of the NCP-X samples phosphidized with the NCG-X precursors. After the phosphidation process, the resulting NCP-X samples were spherical in shape compared to the spherical NCG-X precursors used as the starting materials. Furthermore, from the EDS images of the NCP-X samples, the homogeneous distributions of Ni, Co, and P in the spherical electrode particles were confirmed. However, the surfaces of the NCP-X samples were rougher than those of the NCG-X precursors. The rough surface morphology of the NCP-X samples may be due to the doping and phosphidation processes. From the SEM images, the average particle sizes of NCP-0, NCP-5, NCP-10, and NCP-15 were determined as 505, 464, 404, and 361 nm, respectively (Fig. S3). In particular, NCP-15, with the highest Ni content, has the smallest particle size. The nickel glycerate synthesized in the absence of cobalt salt using the same procedure had a smaller average particle size (477 nm) than that of cobalt glycerate (650 nm). This demonstrates that the particle size of NCP-X decreases with increasing Ni dopant concentration (Fig. S4). Furthermore, according to the literature, increasing the amount of dopant can increase the number of nucleation sites, resulting in a reduced particle size [40]. Fig. 1(b) shows the XRD patterns of the NCP-X samples phosphidized with the NCG-X precursors. NCP-0 prepared without Ni doping had a single phase of CoP (PDF 89-2598) with an orthorhombic structure, resulting in XRD peaks at  $31.58^\circ$ ,  $36.31^\circ$ ,  $46.16^\circ$ ,  $48.08^\circ$ ,  $52.13^\circ$ , and  $56.09^\circ$  corresponding to the (011), (111), (112), (211), (103), and (020) planes, respectively [41]. For the NCP samples, the XRD peaks associated with CoP were solely observed in the absence of any Ni-related phases, indicating pure solid solutions [42]. In particular, for a Ni-doped CoP structure as a solid solution, the Ni dopant atoms can occupy the Co sites of the CoP matrix.

However, an excessive amount of Ni dopant may lead to unstable surface states, resulting from structural collapse [43]. DFT results have shown that the (211) plane is more stable than other planes [44]. The activation energy for the dissociation reaction of  $\text{OOH}^*$  as the intermediate produced during OER on the (211) plane is the lowest, indicating the highest activity for the OER. The ratios of Ni:Co for NCP-0, NCP-5, NCP-10, and NCP-15 were determined as 0:100, 4:96, 9:91, and 16:84, respectively, by ICP-OES analysis, in good agreement with the nominal ratios (Fig. 1(c)). The surface atomic concentrations of Ni:Co for NCP-0, NCP-5, NCP-10, and NCP-15 confirmed by XPS analysis were 0:100, 6.4:93.6, 10.8:89.2, and 16.1:83.9, respectively, in agreement with ICP data.

Fig. 2 shows the Co 2p, Ni 2p, and P 2p spectra of the NCP-X samples. For NCP-5, NCP-10, and NCP-15, the XPS peaks in Ni  $2p_{3/2}$  region are present at 853.5, 856.9, and 860.3 eV, corresponding to nickel phosphide (Ni-P), oxidized-Ni (Ni-O), and a satellite peak, respectively (Fig. 2(a)). In particular, the presence of the Ni-P peak indicates the Ni could have combined with P during the phosphidation process, replacing the Co, present in the orthorhombic CoP structure, with Ni. The Co 2p spectrum of NCP-0 was fitted by peaks corresponding to Co-P bonds (778.9 and 793.8 eV), surface oxidized Co (782.0 and 798.17 eV), and satellite peaks (785.1 and 801.9 eV) (Fig. 2(b)). For NCP-10, the characteristic XPS peaks, associated with Co-P, Co-O, and satellite effects, were observed at 779.1/794.2 eV, 782.9/798.6 eV, and 785.9/803.7 eV, respectively. Specifically, when compared to NCP-0 and NCP samples, the XPS peaks were shifted to higher binding energies (Table S1). The higher binding energy shift in the Co 2p spectra of the NCP samples may be attributed to partial electron transfer from Co to Ni because of the electronegativity difference between Co (1.88) and Ni (1.91) [45]. The partially positive charge ( $\delta^+$ ) of Co in doped CoP samples can act as an electrocatalytically active site and promote OER activity [46,47]. For all NCP-X samples, metal-phosphide (M-P) and P-O peaks were observed, as previously mentioned in the literature (Fig. 2(c)) [48]. In particular, the negative shifts of M-P peaks for the NCP samples compared to those of undoped CoP were confirmed. This demonstrates that the introduction of Ni in CoP can modify the electronic structure of CoP and induce a positive charge in Co, enhancing the OER activity [49,50].

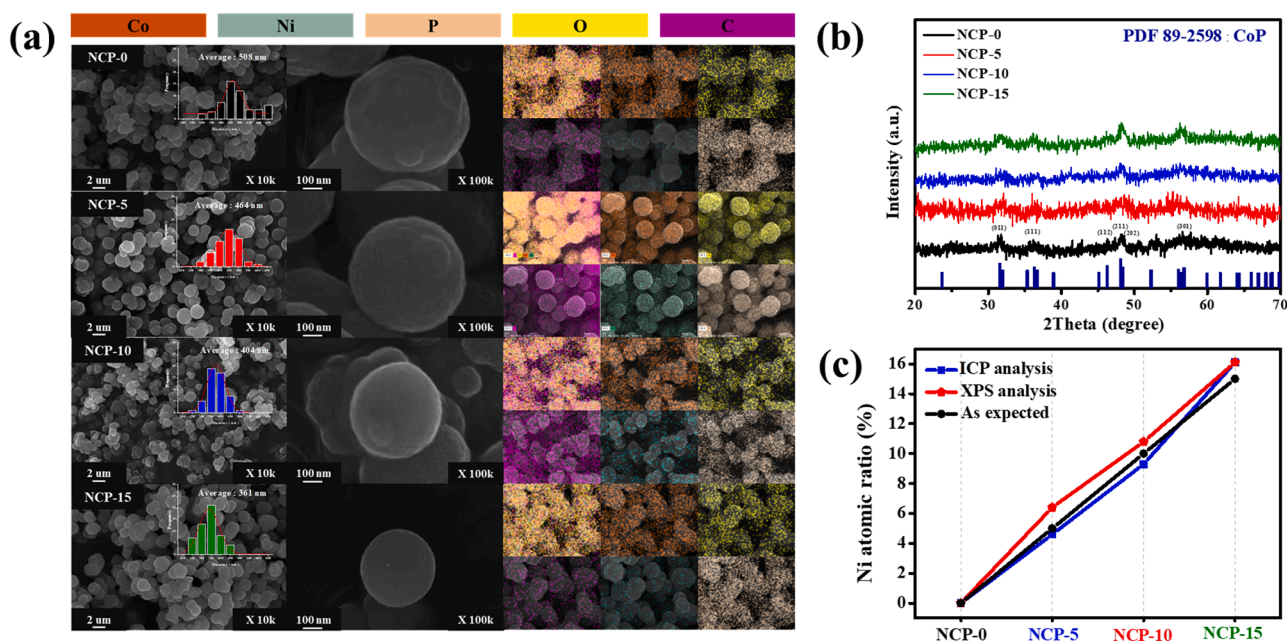


Fig. 1. Physical and chemical properties of NCP-X catalysts: (a) SEM and EDS mapping images; (b) XRD patterns; (c) Ni atomic ratios estimated from XPS and ICP analysis.

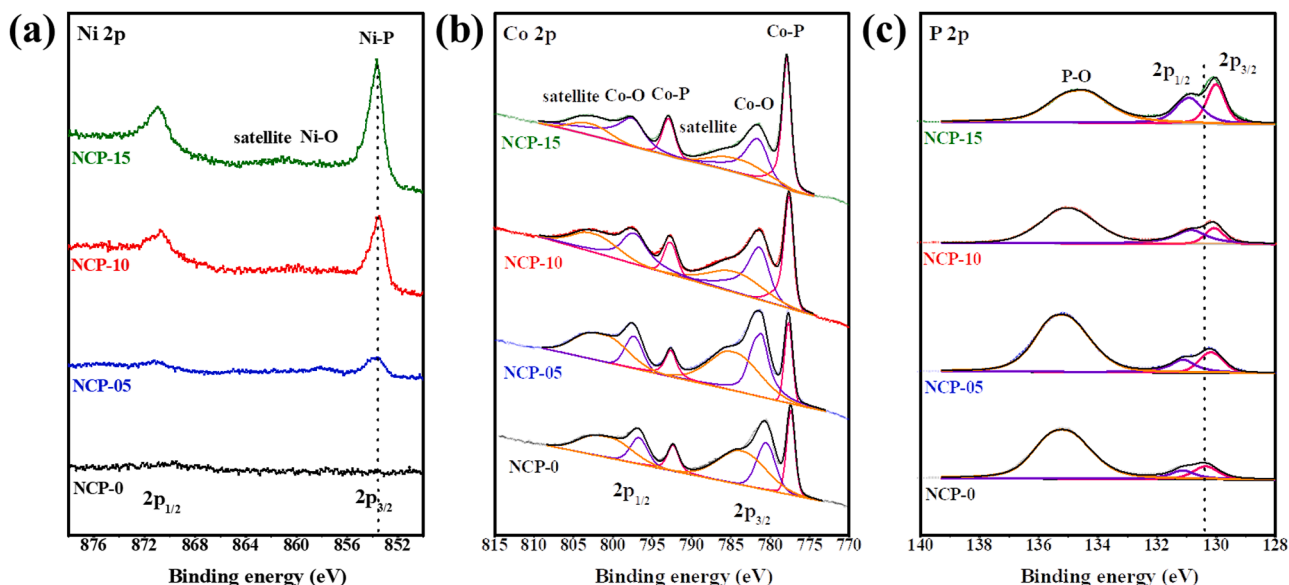


Fig. 2. High resolution XPS profiles for (a) Ni 2p, (b) Co 2p and (c) P 2p for the NCP-X catalysts.

### 3.2. Electrochemical activities of powder-type NCP-X catalysts

Fig. 3(a) shows the LSV curves of the catalysts for the OER in 1.0 M KOH measured at a scan rate of  $5 \text{ mV s}^{-1}$ . The potentials of commercial  $\text{IrO}_2$ , NCP-0, NCP-5, NCP-10, and NCP-15 at a current density of  $10 \text{ mA cm}^{-2}$  are 1.567, 1.609, 1.596, 1.573, and 1.592 V, respectively. The overpotentials of the commercial  $\text{IrO}_2$ , NCP-0, NCP-5, NCP-10, and NCP-15 catalysts were 337, 379, 366, 343, and 362 mV, respectively. Furthermore, the Tafel slopes of NCP-0, NCP-5, NCP-10, and NCP-15 were 92, 93, 84, and 88  $\text{mV dec}^{-1}$ , respectively (Fig. 3(b)). In the electrolytic bath used for the OER tests, the resistance between the reference and working electrodes is the most important factor. To compare the intrinsic activities of the catalysts, the polarization curves are replotted with 85% iR compensation (Fig. 3(c)). The iR-compensated overpotentials of NCP-0, NCP-5, NCP-10, and NCP-15 were 361, 351, 325, and 346 mV, respectively. Compared to NCP-0 (undoped CoP structure), the Ni-doped catalysts had the lower overpotentials and Tafel

slopes, corresponding to higher electrocatalytic activity for the OER. To evaluate the charge-transfer resistance ( $R_{ct}$ ) of the catalysts toward the OER, EIS analysis was performed at 1.6 V over the frequency range of 100 kHz – 100 mHz (Fig. 3(d)). The  $R_{ct}$  values of NCP-0, NCP-5, NCP-10, and NCP-15 are 32, 26, 20, and 21  $\Omega$ , respectively, indicating improved charge transfer properties of the Ni-doped catalysts. The introduction of the Ni dopant in the CoP structure may induce partially oxidized Co ( $\delta +$ ) with an increase in the number of active site and vacancies, thereby promoting electron transport [51]. Furthermore, Ni dopants can act as active sites to improve OER performance. However, excessive Ni doping can produce an excessive number of vacancies and disturb electron transport, resulting in deteriorated OER activity [52]. Thus, the dopant content must be optimized to achieve a catalyst with appropriated OER performance.

The ECSA values of the catalysts were determined by measuring the differences in the current density ( $\Delta j$ ) at 0.9 V vs. RHE as follows [28]:

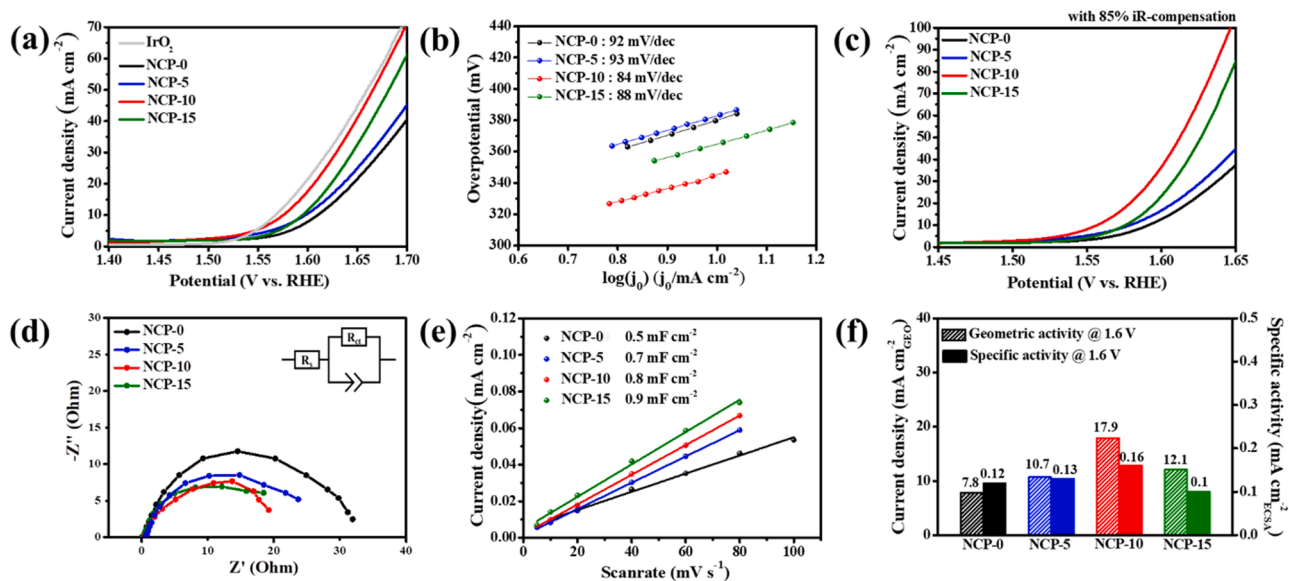


Fig. 3. (a) OER polarization curves without iR-correction, (b) Tafel plots, (c) OER polarization curves with iR-correction, (d) Nyquist plots, (e) double-layer capacitances (Cdl), and (f) comparison of geometric activities and specific activities for the NCP-X catalysts.

$$C_{dl} = \frac{d(\Delta j/2)}{(dV/dt)} \quad (10)$$

$$ECSA(\text{cm}^2) = \frac{C_{dl}}{C_s} \quad (11)$$

where  $C_{dl}$  is the double layer capacitance,  $dV/dt$  is the scan rate, and  $C_s$  is the specific capacitance of  $0.04 \text{ mF cm}^{-2}$  per unit area in an alkaline solution. In particular, the  $\Delta j$  values were measured in the non-faraday potential region, that is,  $0.8\text{--}1.0 \text{ V}$  vs. RHE. The ECSA values of the NCP-0, NCP-5, NCP-10, and NCP-15 are  $12.5$ ,  $17.5$ ,  $20.0$  and  $22.5 \text{ cm}^2$ , respectively (Fig. 3(e)). With increasing Ni content, the ECSA gradually increased due to the decrease in the average particle size (as observed by SEM image (Fig. 1(a))). The higher ECSA of the NCP samples due to doping can significantly increase OER activity. The geometric and specific activities of the samples for OER acquired at  $1.6 \text{ V}$  are compared in Fig. 3(f). Specifically, the current densities measured on the basis of active area, i.e., the geometric activities, for NCP-0, NCP-5, NCP-10, and NCP-15 are  $7.8$ ,  $10.7$ ,  $17.9$ , and  $12.1 \text{ mA cm}^{-2}$ , respectively. It has been reported that the surface electrocatalytic activity can directly dependent on the active area. The specific activities for NCP-0, NCP-5, NCP-10, and NCP-15 are  $0.12$ ,  $0.13$ ,  $0.16$ , and  $0.10 \text{ mA cm}^{-2}$ , respectively. This indicates that for the same active area, appropriate Ni doping enhances the intrinsic electrocatalytic properties of CoP [53].

### 3.3. Theoretical calculations of NCP-X catalysts

Ab initio simulations were used to confirm the effect of Ni doping on the OER performance of CoP. The surface structures of Co-P, NCP-10 and

Ni-P are shown in Fig. 4(a). Based on the structural analysis results, all calculations were optimized in shape. First, the total density of states (TDOS) of the Co-P, NCP-10, and Ni-P catalysts was analyzed to obtain a profound understanding of Ni doping (Fig. 4(b)). All of the studied catalysts have metallic behavior without energy band gaps, resulting in high electrical conductivity. The addition of Ni to Co-P can induce the mixing of the electronic structures between the Ni 3d and P 3p, Co 3d states, gradually increasing the energy density at the Fermi level with increasing Ni content. The charge transfer between the dopant and matrix can modify the electronic density at the Fermi level, which may directly affect the electrical conductivity [54]. In particular, the increased density of charge carriers near the Fermi level may be related to the fast charge-transfer rate. Hence, the modified electronic structure of the NCP-10 catalyst is thought to be the origin of high current density, low Tafel slope, and low  $R_{ct}$  [5]. Furthermore, the  $\Delta G$  for each step in the OER was calculated to investigate the OER performance of the NCP-X catalysts with different Ni doping contents. Four electrons are involved in the complete OER with various reaction intermediates ( $^*\text{OH}$ ,  $^*\text{O}$ , and  $^*\text{OOH}$ ) present on the catalyst surfaces (Eqs.(4)–(7), Fig. 4(c)). The modeling was performed using  $\text{Co}_{1-x}\text{Ni}_x\text{P}$  ( $x = 0, 0.04, 0.07$  and  $0.14$ ), which gives compositions similar to those of the as-synthesized catalysts. The intermediates are adsorbed onto the Co, P, and Ni sites of the catalysts (Fig. S5–S8). The optimized  $\Delta G$  values for each step of the OER are shown in Fig. 4(d). For undoped CoP, both Co and P acted as active sites and the oxidation of  $^*\text{O}$  to  $^*\text{OOH}$  (step (3)) was the rate-determining step in OER. However, for NCP catalysts, the formation energy of  $^*\text{OOH}$  decreased with increasing Ni content. For  $(\text{Co}_{0.86}\text{Ni}_{0.14})\text{P}$ , the oxidation of  $^*\text{OH}$  to  $^*\text{O}$  (step (2)) was determined to be the rate-determining step with a significantly lower energy barrier [55]. The

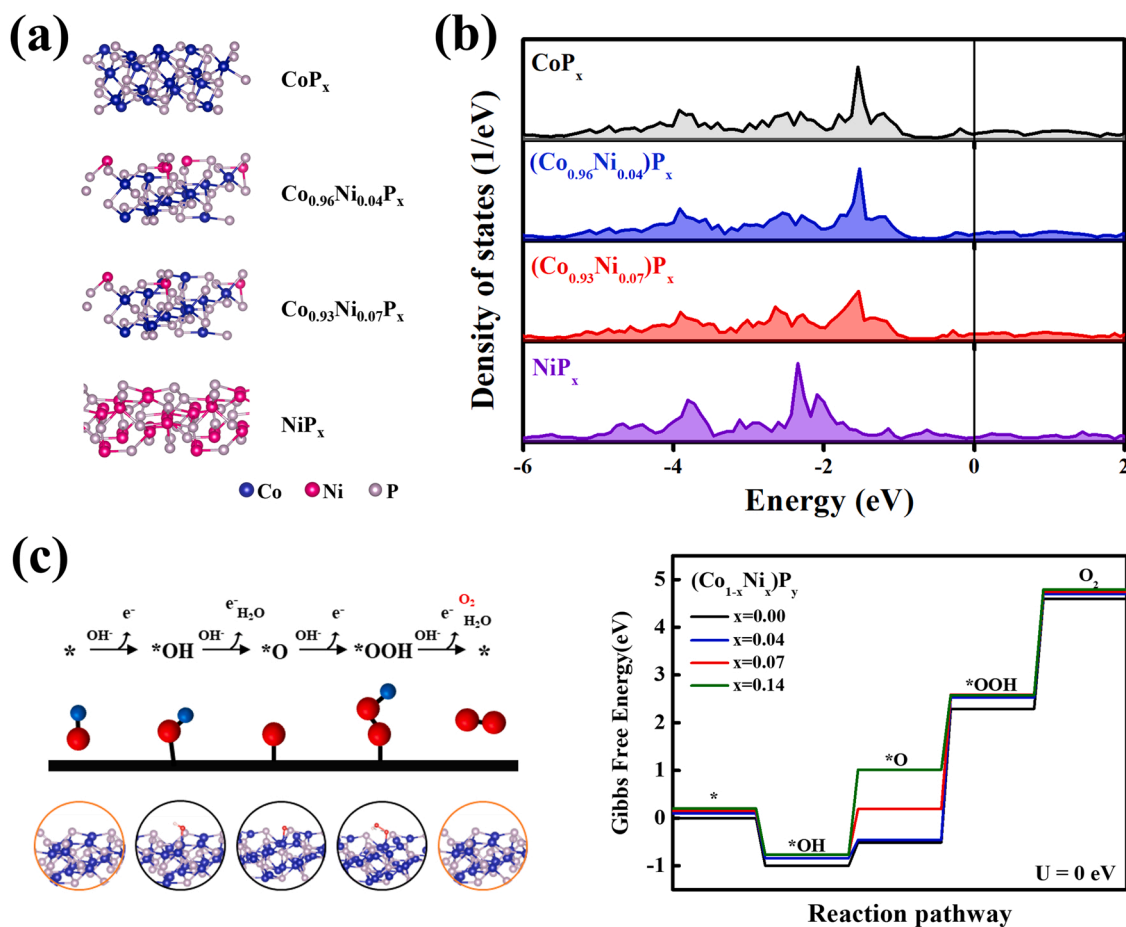


**Fig. 4.** (a) Optimized atomic structures and (b) total density of states diagrams of  $\text{CoP}_x$ ,  $\text{Co}_{1-x}\text{Ni}_x\text{P}$  and  $\text{NiP}_x$ . (c) Free energy diagrams for the OER at 0 and  $1.23 \text{ V}$  vs. RHE on  $\text{Co}_{1-x}\text{Ni}_x\text{P}$  ( $x = 0, 0.04, 0.07$  and  $0.14$ ) (211) facets.

addition of Ni to CoP may enhance the electron transfer and affect the adsorption of OER intermediates, inducing the formation of stable  $^*OOH$  and reducing the overpotential of step (3). With increasing Ni content, the electrocatalytic activity of Co increases, whereas those of Ni and P decrease. As discussed with respect to the XPS results, the addition of Ni to CoP resulted in an increased proportion of  $Co^{3+}$ , resulting in the negative charge transfer from Ni to P. The higher electronic density of P can decrease the adsorption of  $OH^-$ , thereby deteriorating OER activity.

Furthermore, pure Ni-P does not form  $^*OOH$ , indicating its poor OER activity. In the half-cell test, Ni-P gave an overpotential of  $> 500$  mV, i. e., a very low OER activity, which is in agreement with the DFT results (Fig. S9). Hence, appropriate Ni doping can enhance the electrocatalytic activity of Co-P whereas excessive doping can deteriorate the activity, approaching the properties Ni-P. Therefore, the amount of Ni dopant in Co-P must be optimized. In this study, NCP-10 with the optimal Ni content had the best OER performance using electrochemical half-cell

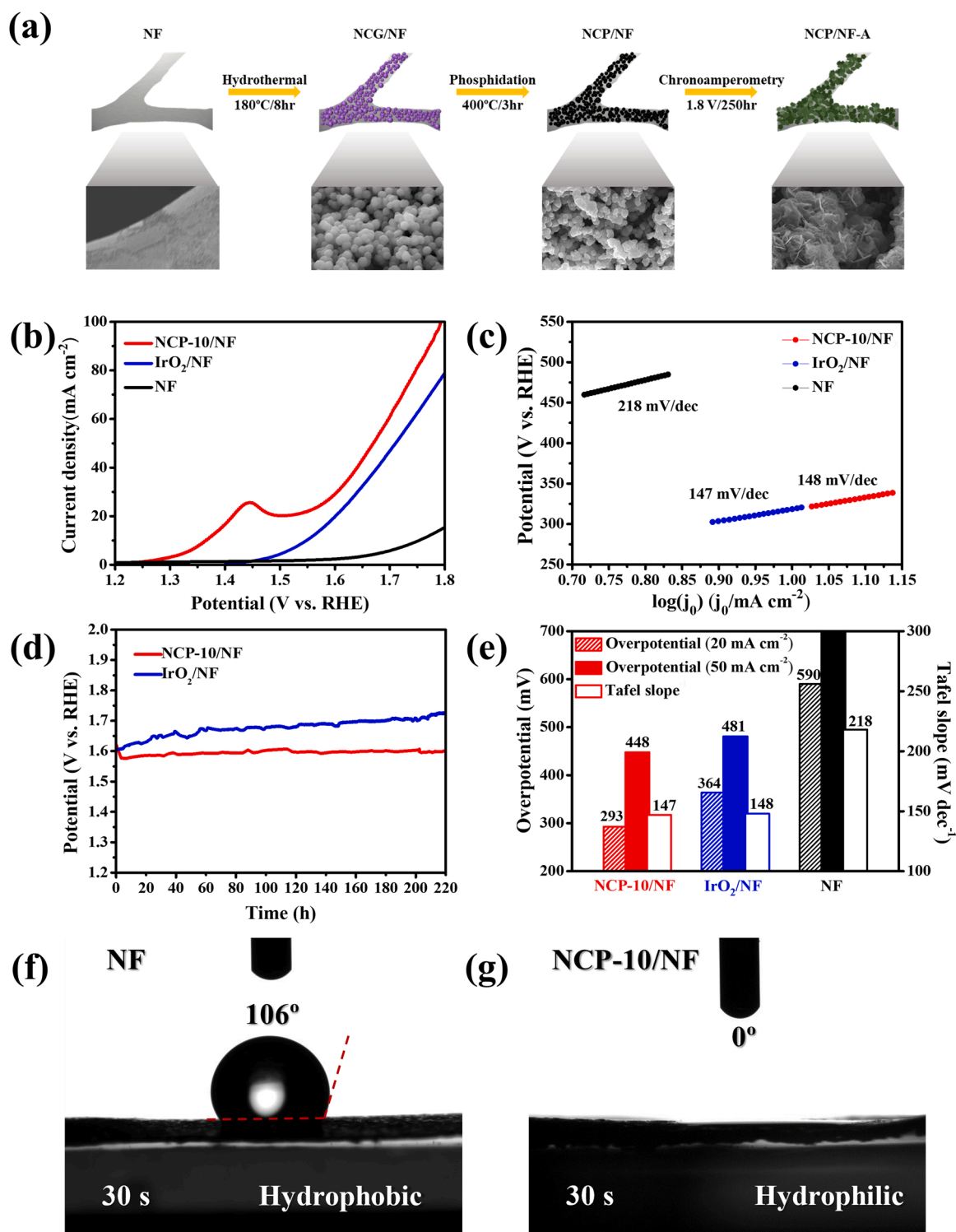


**Fig. 5.** (a) Preparation procedure of NCP-10/NF, (b) OER polarization curves, (c) Tafel plots, (d) time-dependent potential curves and (e) activities at 20 and 50  $mA\ cm^{-2}$  for catalysts loading on Ni foam (NCP-10/NF,  $IrO_2/NF$  and bare NF). (f) Contact angles of NCP-10/NF and (g) bare NF.

tests.

### 3.4. Structure characterization and electrochemical performances of NCP/NF

Glassy carbon electrodes were used to evaluate the intrinsic catalytic properties of the NCP-X samples with the few extrinsic variables affecting the catalysis. However, for the application of the catalysts to a practical electrolyzer, three-dimensional NF as an electrically conductive and binder-free substrate was used, which are designed to reduce the charge-transfer losses and facilitate gas emission while providing good with the electrolyte. The NCG precursor, which was obtained via a hydrothermal process, was homogeneously deposited on an NF substrate (NCG/NF) (Fig. 5(a)). Subsequently, NCG/NF was transformed through a phosphidation process to NCP/NF. The NCP on the NCP/NF has a smaller average particle size ( $\sim 436$  nm) than the NCP prepared without NF (Fig. S10). The electrodes deposited on the NF substrate were fabricated using a dip-coating method with  $\text{IrO}_2$ , which is a representative OER catalyst ( $\text{IrO}_2/\text{NF}$ ). To further evaluate the OER performance, LSV curves and the Tafel slopes of NCP-10/NF,  $\text{IrO}_2/\text{NF}$ , and NF were obtained using a three-electrode electrochemical cell in 1.0 M KOH at a scan rate of  $5 \text{ mV s}^{-1}$ , as shown in Figs. 5(b) and 5(c), respectively. The overpotentials of NCP-10/NF and  $\text{IrO}_2/\text{NF}$  measured at 20 and  $50 \text{ mA cm}^{-2}$  are 293/446 and 364/481 mV, respectively. The Tafel slopes of NCP-10/NF,  $\text{IrO}_2/\text{NF}$ , and NF are 147, 148, and  $218 \text{ mV dec}^{-1}$ , respectively. Compared to  $\text{IrO}_2/\text{NF}$ , NCP-10/NF (prepared by heating a

precursor deposited on NF without a binder) has improved OER performance because homogeneous deposition was achieved without an insulating binder, resulting in a constant current density of  $20 \text{ mA cm}^{-2}$  over 220 h (Figs. 5(d) and 5(e)). During 220 h-stability test, the overpotentials of  $\text{IrO}_2/\text{NF}$  and NCP-10/NF were increased to 494 mV and maintained to 370 mV, respectively. The significantly enhanced stability of NCP-10/NF may be attributed to the transition to stable Ni-Co hydroxide/oxyhydroxide. This indicates that the NF surface for NCP-10/NF changed into super-hydrophilic, which can facilitate the removal of bubble on the catalyst layers and improve the contact with reactants (Fig. 5(f) and 5(g)) [56]. The catalyst deposited on an NF electrode with a relatively low density and porous structure achieves faster emission of  $\text{O}_2$  gas generated during the OER compared to that of the catalyst deposited on a glassy carbon electrode. Furthermore, the NF structure is similar to that of the gas diffusion layer used in a single cell test. Thus, the OER test using the NF electrode can be regarded as an actual single test. When NCP-10/NF was used as the working electrode, the system maintained a constant overpotential for 220 h. After the stability test, it was observed that the spherical NCP-10 particles had been transformed into plate-like shapes (Fig. S10). According to the Pourbaix diagrams of Co and Ni and results in the literature, metal hydroxides can be stable as the main phases in strong alkaline conditions. Hence, the surface of NCP-10 could be transformed into Ni/Co hydroxides, which are well-known to have plate morphologies.

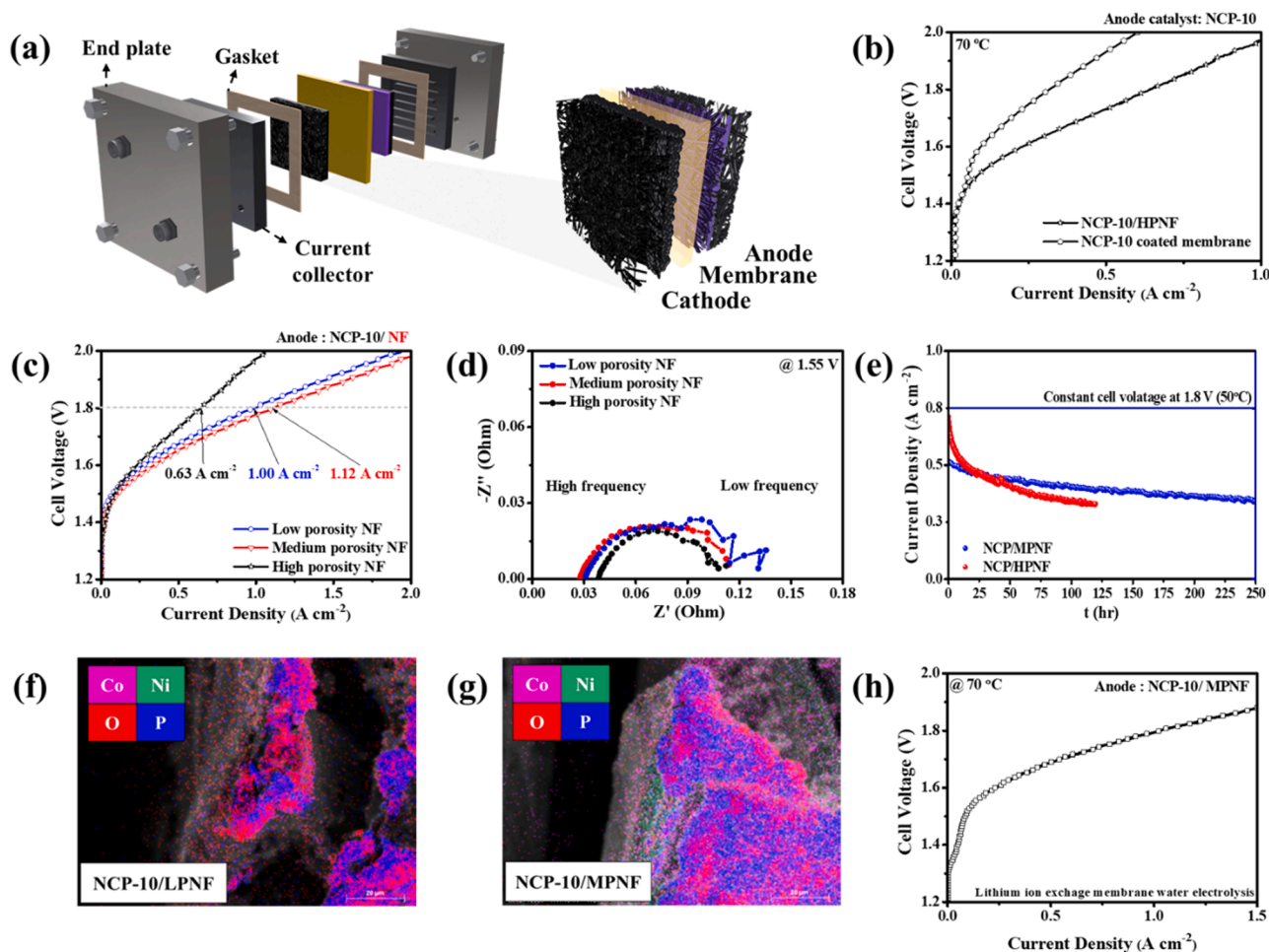


**Fig. 6.** (a) Schematic diagram of the AEMWE cell and (b) polarization curves measured using CCM and CCS-based MEAs with the NCP-10 catalyst. (c) Polarization curves, (d) Nyquist plots, and (e) long term stability test of NCP-10 catalysts on NF with various porosities (NCP-10/HPNF, MPNF and LPNF). SEM images of (f) NCP-10/LPNF and (g) NCP-10/MPNF after stability tests. (h) Polarization curves of a single cell with NCP-10/MPNF for lithium-ion exchange membrane WE.

### 3.5. Performance comparison of AEMWE and LEMWE with NCP/NF

Fig. 6 shows the full cell test results obtained using NCP-10/NF as the anode. The AEM electrolyzer consists of a current collector at the cathode, a gas diffusion electrode for the HER, a membrane, an anode catalyst deposited on NF for the OER, gas diffusion layer, and current collector at the anode (Fig. 6(a)). First, for the evaluation of full cells, a catalyst-coated membrane (CCM)-based MEA (CCM-MEA) was fabricated using a powder-type NCP-10 anode catalyst. Second, a catalyst-coated substrate (CCS)-based MEA (CCS-MEA) was fabricated with NCP-10 deposited on HPNF (NCP-10/HPNF). The polarization curves of the full cells with CCM- and CCS-based MEAs are compared in Fig. 6(b). The performance of the full cell with the CCS-MEA is significantly superior to that of the cell with the CCM-MEA. The catalyst layer formed in the CCM could be settled with an AEM membrane thereby resulting in high ionic conduction. However, the high density of the catalyst layer can obstruct gas emission and electrolyte influx. Recently, instead of high-density catalyst layers, catalyst layers with high permeability have been intensively developed by manipulating the morphologies of the substrates and/or catalysts [23,57]. In general, foam-type electrodes with rough surfaces can damage the membrane surface and easily form pinholes. In this study, 8–10 wt% binder was ultrasonically sprayed on a membrane to prevent such damage to the membrane (Fig. S11). Furthermore, the introduction of a second binder can suppress the catalyst loss, that occurs during the OER. The CCS-MEA fabricated with a binder achieved a five-fold increase in performance compared to the CCM-MEA fabricated without a binder. Furthermore, after the 24 h-stability test, the membrane in the CCS-MEA fabricated with the binder was less damaged than that in the CCM-MEA (Fig. S11). NCP-10 anode catalysts ( $2.8\text{--}3.0\text{ mg cm}^{-2}$ ) were deposited on NF with low, medium, and high porosities (NCP-10/LPNF, NCP-10/MPNF, and NCP-10/HPNF) to investigate the influence of the substrate porosity on the cell performance. The polarization curves of the full cells obtained at  $70^\circ\text{C}$  with NCP-10/LPNF, NCP-10/MPNF, and NCP-10/HPNF are compared in Fig. 6(c). The current densities of NCP-10/LPNF, NCP-10/MPNF, and NCP-10/HPNF measured at 1.8 V are 1.00, 1.12, and  $0.63\text{ A cm}^{-2}$ , respectively. The high-frequency impedance values of NCP-10/LPNF, NCP-10/MPNF, and NCP-10/HPNF measured at 1.55 V using EIS are determined to be 0.030, 0.028, and  $0.039\ \Omega$ , respectively (Fig. 6(d)). The high-frequency impedance is a measure of the internal ohmic resistance resulting from the membrane ionic conductivity, material, and contact resistances. Because the same experimental conditions were used, except for the NF porosity, the contact resistance caused by the contact area and difference in porosity predominantly determine the high-frequency impedance. Hence, the highest contact resistance of HPNF may result from the lowest contact area induced by its highest porosity. A catalyst deposited on a substrate with an appropriately high porosity can deliver improved cell performance, which may facilitate the transport of both reactant and products because of the reduced density of the catalyst layer. However, an excessively high substrate porosity can increase the contact resistance, thereby deteriorating cell performance. Stability tests of the cells with NCP-10/LPNF and NCP-10/MPNF were performed at a constant cell voltage of 1.8 V for 250 h (Fig. 6(e)). The current reduction rates of the cells with NCP-10/LPNF and NCP-10/MPNF are 0.64 and  $2.8\text{ mA cm}^{-2}\text{ hr}^{-1}$ , respectively, indicating the superior stability of NCP-10/LPNF compared to NCP-10/MPNF. After a 100 h-stability test, the surface states of the catalyst layers were investigated by SEM and EDS (Figs. 6(f) and 6(g)). The presence of O as well as P in the surface was confirmed, indicating an oxidized surface. Mercury porosimetry analysis of LPNF and MPNF gave specific surface areas of 7.9 and  $13.7\text{ m}^2\text{ g}^{-1}$ , respectively (Table S2). MPNF with higher porosity and specific surface area (i. e., reaction area) than LPNF promotes the emission of oxygen generated during the OER, enhancing the initial performance. However, the surface oxidation of Ni, resulting from the alkaline solution and high operating current density can deteriorate the OER performance. The

significant content of oxygen in both NCP-10/LPNF and NCP-10/MPNF indicates the transition of the metal phosphide phases to surface oxidized phases, such as hydroxides or oxides with relatively low electrical conductivities (Fig. S12 and S13). During a 250 h-stability test, the NCP-10/NF as highly stable (Table S3). EDS analysis of the catalyst region in NCP-10/MPNF were performed before and after the stability test. In addition, the surface states of the catalysts after the OER test were investigated by XPS analysis (Fig. S14). After the OER stability test, the Ni- and Co-related peaks were shifted to lower binding energies, indicating the increased portions of  $\text{Co}^{3+}$  and  $\text{Ni}^{3+}$ . This represents the transition of the catalyst surface to  $\text{CoOOH}/\text{NiOOH}$  as the more stable species during the oxidation process [35,58–61]. Specifically, after the stability test, the signal intensity of the P 2p peak was significantly decreased. Furthermore, when compared with O 1s spectra before and after the stability test, the intensities of O-H and P-O peaks were increased and decreased, respectively. Also, this indicates the surface transition of NCP-10 to metal oxyhydroxides/hydroxides [35,58–61]. The P-related signal intensity after 250 h-stability test is lower than that before testing, whereas the O-related signal intensity is higher after the stability test. According to the literature, the surface regions of metal phosphides can be transformed into metal hydroxides during electrochemical oxidation reactions such as the OER [62–64]. However, bare NF showed no noticeable surface variations after the stability test, indicating the surface change resulting from the catalyst (Fig. S15). NCP-10/MPNF applied to LEMWE delivered a high current density of  $1.03\text{ A cm}^{-2}$  at 1.8 V (Fig. 6(h)). This demonstrates that NCP-10 is suitable for use as a non-precious metal catalyst in both LEMWE and AEMWE systems.

## 4. Conclusion

Here, spherical Ni-doped CoP anode catalysts (Ni: 5–15 at%) were obtained using hydrothermal and phosphidation processes. The Ni dopant acted as a heterogeneous nucleation sites to reduce the average particle sizes and increase the active area of the catalyst. The partial oxidation of Co resulting from Ni with relatively high electronegativity might increase the OER electrocatalytic activity. However, excessive Ni doping of CoP could destroy the stable orthorhombic structure and induce excessive vacancy formation, thereby hindering electron transport and deteriorating the OER activity and stability. NCP-10 with the optimal Ni content exhibited the best OER performance in half and single cells, owing to its lowest energy barrier for the rate-determining step in the OER (of all catalysts tested here). Furthermore, the porosity of the NF used as a substrate for NCP-10 could be optimized to improve electrocatalytic performance and stability of the electrodes.

### CRedit authorship contribution statement

**Deok-Hye Park:** Conceptualization, Methodology, Formal analysis, Data curation, Writing – original draft. **Min-Ha Kim, Myungjae Kim:** Investigation, Data curation. **Jeong-Hyeon Byeon, Jae-Sung Jang, Ji-Hwan Kim, Da-Mi Lim, Seon-Ha Park, Yun-Hui Gu:** Data curation. **Jiwoong Kim, Kyung-Won Park:** Conceptualization, Supervision, Writing – review & editing.

### Declaration of Competing Interest

The authors declare that they have no known competing financial interests or personal relationships that could have appeared to influence the work reported in this paper.

### Data availability

Data will be made available on request.

## Acknowledgments

This research was supported by the National Research Foundation of Korea (2019M3E6A1104186, 2020R1A6A1A03044977) and the National Research Council of Science & Technology (NST) grant by the Korea government (MSIT) (No. CAP22071-000).

## Appendix A. Supporting information

Supplementary data associated with this article can be found in the online version at [doi:10.1016/j.apcatb.2023.122444](https://doi.org/10.1016/j.apcatb.2023.122444).

## References

- [1] A. Buttler, H. Spliethoff, Current status of water electrolysis for energy storage, grid balancing and sector coupling via power-to-gas and power-to-liquids: a review, *Renew. Sustain. Energy Rev.* 82 (2018) 2440–2454.
- [2] F.M. Sapountzi, J.M. Gracia, C.J. Weststrate, H.O.A. Fredriksson, J. W. Niemantsverdriet, Electrocatalysts for the generation of hydrogen, oxygen and synthesis gas, *Prog. Energy Combust. Sci.* 58 (2017) 1–35.
- [3] M. Yu, E. Budiyanto, H. Tuysuz, Principles of water electrolysis and recent progress in cobalt-, nickel-, and iron-based oxides for the oxygen evolution reaction, *Angew. Chem. Int. Ed.* 61 (2022) e202103824.
- [4] N. Du, C. Roy, R. Peach, M. Turnbull, S. Thiele, C. Bock, Anion-exchange membrane water electrolyzers, *Chem. Rev.* 122 (2022) 11830–11895.
- [5] X. Hu, S. Zhang, J. Sun, L. Yu, X. Qian, R. Hu, Y. Wang, H. Zhao, J. Zhu, 2D Fe-containing cobalt phosphide/cobalt oxide lateral heterostructure with enhanced activity for oxygen evolution reaction, *Nano Energy* 56 (2019) 109–117.
- [6] M. Plevová, J. Hnát, K. Bouzek, Electrocatalysts for the oxygen evolution reaction in alkaline and neutral media. A comparative review, *J. Power Sources* 507 (2021), 230072.
- [7] H. Yang, M. Driess, P.W. Menezes, Self-supported electrocatalysts for practical water electrolysis, *Adv. Energy Mater.* 11 (2021) 2102074.
- [8] L. Yang, R. Liu, L. Jiao, Electronic redistribution: construction and modulation of interface engineering on CoP for enhancing overall water splitting, *Adv. Funct. Mater.* 30 (2020) 1909618.
- [9] A. Parra-Puerto, K.L. Ng, K. Fahy, A.E. Goode, M.P. Ryan, A. Kucernak, Supported transition metal phosphides: activity survey for HER, ORR, OER, and corrosion resistance in acid and alkaline electrolytes, *ACS Catal.* 9 (2019) 11515–11529.
- [10] T. Zhang, K.N. Yang, C. Wang, S.Y. Li, Q.Q. Zhang, X.J. Chang, J.T. Li, S.M. Li, S. F. Jia, J.B. Wang, L. Fu, Nanometric  $\text{Ni}_5\text{P}_4$  clusters nested on  $\text{NiCo}_2\text{O}_4$  for efficient hydrogen production via alkaline water electrolysis, *Adv. Energy Mater.* 8 (2018) 1801690.
- [11] S. Anantharaj, J. Kennedy, S. Kundu, Microwave-initiated facile formation of  $\text{Ni}_3\text{Se}_4$  nanoassemblies for enhanced and stable water splitting in neutral and alkaline media, *ACS Appl. Mater. Interfaces* 9 (2017) 8714–8728.
- [12] Y.S. Park, J. Jeong, Y. Noh, M.J. Jang, J. Lee, K.H. Lee, D.C. Lim, M.H. Seo, W. B. Kim, J. Yang, S.M. Choi, Commercial anion exchange membrane water electrolyzer stack through non-precious metal electrocatalysts, *Appl. Catal. B* 292 (2021), 120170.
- [13] Y. Wang, B. Kong, D. Zhao, H. Wang, C. Selomulya, Strategies for developing transition metal phosphides as heterogeneous electrocatalysts for water splitting, *Nano Today* 15 (2017) 26–55.
- [14] Y. Wang, S. Zhao, Y. Zhu, R. Qiu, T. Gengenbach, Y. Liu, L. Zu, H. Mao, H. Wang, J. Tang, D. Zhao, C. Selomulya, Three-dimensional hierarchical porous nanotubes derived from metal-organic frameworks for highly efficient overall water splitting, *iScience* 23 (2020), 100761.
- [15] H. Qiao, X. Wang, Q. Dong, H. Zheng, G. Chen, M. Hong, C.-P. Yang, M. Wu, K. He, L. Hu, A high-entropy phosphate catalyst for oxygen evolution reaction, *Nano Energy* 86 (2021), 106029.
- [16] G. Zhang, Y. Li, X. Xiao, Y. Shan, Y. Bai, H.G. Xue, H. Pang, Z. Tian, Q. Xu, In situ anchoring polymetallic phosphide nanoparticles within porous prussian blue analogue nanocages for boosting oxygen evolution catalysis, *Nano Lett.* 21 (2021) 3016–3025.
- [17] Y.N. Wang, Z.J. Yang, D.H. Yang, L. Zhao, X.R. Shi, G. Yang, B.H. Han,  $\text{FeCoP}_2$  nanoparticles embedded in N and P Co-doped hierarchically porous carbon for efficient electrocatalytic water splitting, *ACS Appl. Mater. Interfaces* 13 (2021) 8832–8843.
- [18] D. Chen, R. Lu, Z. Pu, J. Zhu, H.-W. Li, F. Liu, S. Hu, X. Luo, J. Wu, Y. Zhao, S. Mu, Ru-doped 3D flower-like bimetallic phosphide with a climbing effect on overall water splitting, *Appl. Catal. B* 279 (2020), 119396.
- [19] J.-L. Yang, J.-M. Cao, X.-X. Zhao, K.-Y. Zhang, S.-H. Zheng, Z.-Y. Gu, X.-L. Wu, Advanced aqueous proton batteries: working mechanism, key materials, challenges and prospects, *EnergyChem* 4 (2022), 100092.
- [20] X. Li, X. Yang, H. Xue, H. Pang, Q. Xu, Metal-organic frameworks as a platform for clean energy applications, *EnergyChem* 2 (2020), 100027.
- [21] P. Geng, L. Wang, M. Du, Y. Bai, W. Li, Y. Liu, S. Chen, P. Braunstein, Q. Xu, H. Pang, MIL-96-Al for Li-S batteries: shape or size? *Adv. Mater.* 34 (2022), e2107836.
- [22] W. Li, X. Guo, P. Geng, M. Du, Q. Jing, X. Chen, G. Zhang, H. Li, Q. Xu, P. Braunstein, H. Pang, Rational design and general synthesis of multimetallic metal-organic framework nano-octahedra for enhanced Li-S battery, *Adv. Mater.* 33 (2021) 2105163.
- [23] W. Zheng, M. Liu, L.Y.S. Lee, Best practices in using foam-type electrodes for electrocatalytic performance benchmark, *ACS Energy Lett.* 5 (2020) 3260–3264.
- [24] S. Jiang, T. Shi, H. Long, Y. Sun, W. Zhou, Z. Tang, High-performance binder-free supercapacitor electrode by direct growth of cobalt-manganese composite oxide nanostructures on nickel foam, *Nanoscale Res. Lett.* 9 (2014) 1–8.
- [25] D. Xiong, C. Lu, C. Chen, J. Wang, Y. Kong, T. Liu, S. Ying, F.-Y. Yi, CoFeP nanocube-arrays based on Prussian blue analogues for accelerated oxygen evolution electrocatalysis, *J. Power Sources* 520 (2022), 230884.
- [26] M. Yu, G. Moon, E. Bill, H. Tüysüz, Optimizing Ni-Fe oxide electrocatalysts for oxygen evolution reaction by using hard templating as a toolbox, *ACS Appl. Energy Mater.* 2 (2019) 1199–1209.
- [27] N.L.W. Septiani, Y.V. Kaneti, K.B. Fathoni, Y. Guo, Y. Ide, B. Yulianto, X. Jiang, Nugraha, H.K. Dipojono, D. Golberg, Y. Yamauchi, Tailorable nanoarchitecturing of bimetallic nickel-cobalt hydrogen phosphate via the self-weaving of nanotubes for efficient oxygen evolution, *J. Mater. Chem.* 8 (2020) 3035–3047.
- [28] D.H. Park, M.H. Kim, H.J. Lee, W.J. Lee, J.H. Byeon, J.H. Kim, J.S. Jang, K.W. Park, Development of Ni-Ir oxide composites as oxygen catalysts for an anion-exchange membrane water electrolyzer, *Adv. Mater. Interfaces* 9 (2022) 2102063.
- [29] Y.-S. Lee, Y.-H. Mo, D.-H. Park, H.-J. Lee, W.-J. Lee, H.-S. Park, S.-B. Han, K.-W. Park, Highly efficient lithium-ion exchange membrane water electrolysis, *J. Power Sources* 529 (2022), 231188.
- [30] J. Hafner, Ab-initio simulations of materials using VASP: Density-functional theory and beyond, *J. Comput. Chem.* 29 (2008) 2044–2078.
- [31] A.V. Krukau, O.A. Vydrov, A.F. Izmaylov, G.E. Scuseria, Influence of the exchange screening parameter on the performance of screened hybrid functionals, *J. Chem. Phys.* 125 (2006), 224106.
- [32] J.P. Perdew, K. Burke, M. Ernzerhof, Generalized gradient approximation made simple, *Phys. Rev. Lett.* 77 (1996) 3865.
- [33] G. Kresse, D. Joubert, From ultrasoft pseudopotentials to the projector augmented-wave method, *Phys. Rev. B* 59 (1999) 1758.
- [34] J.K. Nørskov, J. Rossmeisl, A. Logadottir, L. Lindqvist, J.R. Kitchin, T. Bligaard, H. Jonsson, Origin of the overpotential for oxygen reduction at a fuel-cell cathode, *J. Phys. Chem. B* 108 (2004) 17886–17892.
- [35] N.L.W. Septiani, Y.V. Kaneti, K.B. Fathoni, K. Kani, A.E. Allah, B. Yulianto, Nugraha, H.K. Dipojono, Z.A. Alohtman, D. Golberg, Y. Yamauchi, Self-assembly of two-dimensional bimetallic nickel-cobalt phosphate nanoplates into one-dimensional porous chainlike architecture for efficient oxygen evolution reaction, *Chem. Mater.* 32 (2020) 7005–7018.
- [36] T.X. Nguyen, Y.H. Su, C.C. Lin, J. Ruan, J.M. Ting, A. New, High entropy glycerate for high performance oxygen evolution reaction, *Adv. Sci.* 8 (2021) 2002446.
- [37] Y.V. Kaneti, R.R. Salunkhe, N.L. Wulan Septiani, C. Young, X. Jiang, Y.-B. He, Y.-M. Kang, Y. Sugahara, Y. Yamauchi, General template-free strategy for fabricating mesoporous two-dimensional mixed oxide nanosheets via self-deconstruction/reconstruction of monodispersed metal glycerate nanospheres, *J. Mater. Chem.* 6 (2018) 5971–5983.
- [38] Y.V. Kaneti, N.L. Wulan Septiani, I. Saptiama, X. Jiang, B. Yulianto, M.J. A. Shiddiky, N. Fukumitsu, Y.-M. Kang, D. Golberg, Y. Yamauchi, Self-sacrificial templated synthesis of a three-dimensional hierarchical macroporous honeycomb-like  $\text{ZnO}/\text{ZnCo}_2\text{O}_4$  hybrid for carbon monoxide sensing, *J. Mater. Chem.* 7 (2019) 3415–3425.
- [39] X. Guo, J. Liang, L. Wang, Z. Feng, T. Yu, Z. Zhang, Y. Shao, C. Hao, G. Li, Synthesis of Cobalt-Glycerate hierarchical structure and their conversion into hierarchical CoP nanospheres for the hydrogen evolution reaction, *Int. J. Hydrog. Energy* 43 (2018) 2034–2042.
- [40] C. Zhang, Y. Wang, X. Lin, T. Wu, Q. Han, Y. Zhang, L. Han, Effects of A site doping on the crystallization of perovskite films, *J. Mater. Chem.* 9 (2021) 1372–1394.
- [41] R. Jin, X. Li, Y. Sun, H. Shan, L. Fan, D. Li, X. Sun, Metal-organic frameworks-derived  $\text{Co}_2\text{P}/\text{N}-\text{C}@r\text{GO}$  with dual protection layers for improved sodium storage, *ACS Appl. Mater. Interfaces* 10 (2018) 14641–14648.
- [42] L. Yan, L. Cao, P. Dai, X. Gu, D. Liu, L. Li, Y. Wang, X. Zhao, Metal-organic frameworks derived nanotube of nickel-cobalt bimetal phosphides as highly efficient electrocatalysts for overall water splitting, *Adv. Funct. Mater.* 27 (2017) 1703455.
- [43] M. Choi, H. Choi, J. Ahn, Y.T. Kim, Understanding of relationship between dopant and substitutional site to develop novel phase-change materials based on  $\text{In}_3\text{SbTe}_2$ , *Jpn. J. Appl. Phys.* 58 (2019), SBBB02.
- [44] S. Xie, F. Yang, H. Zhang, S. Wang, F. Cheng, X. Lu, Oxygen functionalized CoP nanowires as high-efficient and stable electrocatalyst for oxygen evolution reaction and full water splitting, *J. Electrochem. Soc.* 167 (2020), 124512.
- [45] M.R. Kandel, U.N. Pan, D.R. Paudel, P.P. Dhakal, N.H. Kim, J.H. Lee, Hybridized bimetallic phosphides of Ni-Mo, Co-Mo, and Co-Ni in a single ultrathin-3D-nanosheets for efficient HER and OER in alkaline media, *Compos. B. Eng.* 239 (2022), 109992.
- [46] W.Y. Xia, N. Li, Q.Y. Li, K.H. Ye, C.W. Xu,  $\text{Au-NiCo}_2\text{O}_4$  supported on three-dimensional hierarchical porous graphene-like material for highly effective oxygen evolution reaction, *Sci. Rep.* 6 (2016) 23398.
- [47] C.-C. Lin, C.C.L. McCrory, Effect of chromium doping on electrochemical water oxidation activity by  $\text{Co}_{3-x}\text{Cr}_x\text{O}_4$  spinel catalysts, *ACS Catal.* 7 (2016) 443–451.
- [48] X. Liu, S. Deng, D. Xiao, M. Gong, J. Liang, T. Zhao, T. Shen, D. Wang, Hierarchical Bimetallic Ni-Co-P Microflowers with Ultrathin Nanosheet Arrays for Efficient Hydrogen Evolution Reaction over All pH Values, *ACS Appl. Mater. Interfaces* 11 (2019) 42233–42242.
- [49] J. Zhao, Y. He, J. Wang, J. Zhang, L. Qiu, Y. Chen, C. Zhong, X. Han, Y. Deng, W. Hu, Regulating metal active sites of atomically-thin nickel-doped spinel cobalt

- oxide toward enhanced oxygen electrocatalysis, *Chem. Eng. J.* 435 (2022), 134261.
- [50] S. Ghosh, S.R. Kadam, S. Kolatkar, A. Neyman, C. Singh, A.N. Enyashin, R. Bar-Ziv, M. Bar-Sadan, W. Doping in  $\text{Ni}_{12}\text{P}_5$  as a Platform to Enhance Overall Electrochemical Water Splitting, *ACS Appl. Mater. Interfaces* 14 (2022) 581–589.
- [51] Z. Liu, G. Wang, X. Zhu, Y. Wang, Y. Zou, S. Zang, S. Wang, Optimal geometrical configuration of cobalt cations in spinel oxides to promote oxygen evolution reaction, *Angew. Chem. Int. Ed.* 59 (2020) 4736–4742.
- [52] Y. Liu, N. Ran, R. Ge, J. Liu, W. Li, Y. Chen, L. Feng, R. Che, Porous Mn-doped cobalt phosphide nanosheets as highly active electrocatalysts for oxygen evolution reaction, *Chem. Eng. J.* 425 (2021), 131642.
- [53] R. Wu, B. Xiao, Q. Gao, Y.R. Zheng, X.S. Zheng, J.F. Zhu, M.R. Gao, S.H. Yu, A. Janus, Nickel cobalt phosphide catalyst for high-efficiency neutral-pH water splitting, *Angew. Chem. Int. Ed.* 57 (2018) 15445–15449.
- [54] G. Zhang, G. Wang, Y. Liu, H. Liu, J. Qu, J. Li, Highly active and stable catalysts of phytic acid-derivative transition metal phosphides for full water splitting, *J. Am. Chem. Soc.* 138 (2016) 14686–14693.
- [55] Q. Wang, X. Huang, Z.L. Zhao, M. Wang, B. Xiang, J. Li, Z. Feng, H. Xu, M. Gu, Ultrahigh-Loading of Ir Single Atoms on NiO Matrix to Dramatically Enhance Oxygen Evolution Reaction, *J. Am. Chem. Soc.* 142 (2020) 7425–7433.
- [56] L. Zhang, Z. Hu, H. Li, Q. Ren, Y. Qiu, J. Qu, S. Hu, Nickel foam supported NiO@Ru heterostructure towards high-efficiency overall water splitting, *Chemphyschem* 22 (2021) 1785–1791.
- [57] L. Wan, Z. Xu, Q. Xu, P. Wang, B. Wang, Overall design of novel 3D-ordered MEA with drastically enhanced mass transport for alkaline electrolyzers, *Energy Environ. Sci.* 15 (2022) 1882–1892.
- [58] X. Zhou, Y. Zi, L. Xu, T. Li, J. Yang, J. Tang, Core-shell-structured prussian blue analogues ternary metal phosphides as efficient bifunctional electrocatalysts for OER and HER, *Inorg. Chem.* 60 (2021) 11661–11671.
- [59] P. Bhanja, Y. Kim, B. Paul, J. Lin, S.M. Alshehri, T. Ahamad, Y.V. Kaneti, A. Bhaumik, Y. Yamauchi, Facile synthesis of nanoporous transition metal-based phosphates for oxygen evolution reaction, *ChemCatChem* 12 (2020) 2091–2096.
- [60] P. Bhanja, Y. Kim, B. Paul, Y.V. Kaneti, A.A. Allothman, A. Bhaumik, Y. Yamauchi, Microporous nickel phosphonate derived heteroatom doped nickel oxide and nickel phosphide: efficient electrocatalysts for oxygen evolution reaction, *Chem. Eng. J.* 405 (2021), 126803.
- [61] C. Liu, H. Zhu, Z. Zhang, J. Hao, Y. Wu, J. Guan, S. Lu, F. Duan, M. Zhang, M. Du, Binary nickel iron phosphide composites with oxidized surface groups as efficient electrocatalysts for the oxygen evolution reaction, *Sustain. Energy Fuels* 3 (2019) 3518–3524.
- [62] A. Li, L. Zhang, F. Wang, L. Zhang, L. Li, H. Chen, Z. Wei, Rational design of porous Ni-Co-Fe ternary metal phosphides nanobricks as bifunctional electrocatalysts for efficient overall water splitting, *Appl. Catal. B* 310 (2022), 121353.
- [63] Y. Deng, Y. Cao, Y. Xia, X. Xi, Y. Wang, W. Jiang, D. Yang, A. Dong, T. Li, Self-templated synthesis of CoFeP @ C cage-in-cage superlattices for enhanced electrocatalytic water splitting, *Adv. Energy Mater.* (2022) 2202394.
- [64] D. Chanda, K. Kannan, J. Gautam, M.M. Meshesha, S.G. Jang, V.A. Dinh, B.L. Yang, Effect of the interfacial electronic coupling of nickel-iron sulfide nanosheets with layer  $\text{Ti}_3\text{C}_2$  MXenes as efficient bifunctional electrocatalysts for anion-exchange membrane water electrolysis, *Appl. Catal. B* 321 (2023), 122039.